Dynamic microtubules regulate cellular contractility during T-cell activation

King Lam Hui[a,1] and Arpita Upadhyaya[a,b,2]

[a]Department of Physics, University of Maryland, College Park, MD 20742; and [b]Institute for Physical Science and Technology, University of Maryland, College Park, MD 20742

T-cell receptor (TCR) triggering and subsequent T-cell activation are essential for the adaptive immune response. Recently, multiple lines of evidence have shown that force transduction across the TCR complex is involved during TCR triggering, and that the T cell might use its force-generation machinery to probe the mechanical properties of the opposing antigen-presenting cell, giving rise to different signaling and physiological responses. Mechanistically, actin polymerization and turnover have been shown to be essential for force generation by T cells, but how these actin dynamics are regulated spatiotemporally remains poorly understood. Here, we report that traction forces generated by T cells are regulated by dynamic microtubules (MTs) at the interface. These MTs suppress Rho activation, nonmuscle myosin II bipolar filament assembly, and actin retrograde flow at the T-cell–substrate interface. Our results suggest a novel role of the MT cytoskeleton in regulating force generation during T-cell activation.

mechanobiology | T-cell activation | microtubule | actin | myosin II

T lymphocytes, central players in the adaptive immune response, are activated when T-cell receptors (TCRs) on their surface recognize cognate peptide-major histocompatibility complex (pMHC) expressed on the surface of antigen-presenting cells (APCs). A burst of actin polymerization is triggered upon TCR stimulation (1), leading to an enhancement of the cell/APC contact area as the T cell spreads over the surface of the APC (2) and the formation of a macromolecular protein assembly known as the immunological synapse (IS) (3, 4). Accompanying IS formation, T cells also undergo a rapid polarization of the microtubule (MT) cytoskeleton, within 1–2 min after initial contact, that facilitates directional secretion of cytokines and cytolytic factors toward the APC (5–7). Therefore, the contact zone between T cells and APCs is a site at which the MT and actin cytoskeletons could potentially interact to regulate signaling.

Recent studies have established that T cells generate significant traction stresses at the cell–cell interface, albeit relatively weak compared with adherent cells (8–11). These forces, which peak 5–10 min after stimulation, facilitate T-cell activation, in part, by inducing conformational changes in the TCR–CD3 complex (12–15). Although actin polymerization/depolymerization dynamics are essential for T cells to maintain dynamic traction stresses and to drive calcium influx and integrin affinity maturation (9, 16, 17), the regulatory pathways that control these cytoskeletal forces are not completely understood. In particular, whether and how the polarized MT cytoskeleton interacts with the actin cytoskeleton and regulates force generation at the T-cell–APC contact remain open questions.

MTs in the cell exist in two populations: dynamic/tyrosinated MTs and stable MTs that have undergone posttranslational modifications, including detyrosination and acetylation (18). Previous studies of T-cell activation have elucidated that microtubule-organizing center (MTOC) translocation is associated with the formation of stable MTs. For example, overexpression of histone deacetylase 6, which deacetylates tubulin, results in defective MTOC translocation (19). A similar phenotype is observed when

formins (including DIA1, FMNL1, and INF2), which are capable of inducing MT acetylation (20), are depleted (5, 21). On the other hand, the biological functions of the MT cytoskeleton after the MTOC has translocated are less understood. In adherent cells, dynamic MTs appear to have an indirect role in force generation, engaging in a negative feedback loop with focal adhesion assembly (22, 23), and global MT depolymerization induces an increase in traction forces (24). Here, we combine results from traction force microscopy (TFM) and quantitative analysis of cytoskeletal dynamics to elucidate a role for MTs in the regulation of T-cell forces during activation. We find that MTs at the T-cell contact are dynamic and undergo growth and catastrophes as shown earlier (25, 26), which suppresses Rho-associated contractility and actin flow, regulating force generation during activation. Our results thus suggest a key role for the cross-talk between these two cytoskeletal components during T-cell activation, which could be of general importance for understanding mechanisms underlying force generation in other cellular systems.

Results

MT Network Forms a Radially Emanating Dynamic Array During T-Cell Activation. To study cytoskeletal dynamics during signaling activation, we activated E6-1 Jurkat T cells on coverslips coated with anti-CD3∈, as described earlier (2). To characterize MT dynamics in live cells, we transfected EGFP-actin–expressing Jurkat cells with TagRFP-T–β-tubulin and conducted dual-color imaging in total internal reflection fluorescence (TIRF) mode. After contact with the stimulatory surface, MT growth/catastrophe was sustained for at least 10 min (Movie S1). To visualize the MT and actin cytoskeletons simultaneously with high spatial resolution, we permeabilized E6-1 Jurkat cells after 10 min of anti-CD3 stimulation on coverslips fixed and stained for tubulin and F-actin (27).

Significance

T-cell activation is an essential event in the adaptive immune response to fight against infections. T cells were recently shown to be mechanosensitive, and to exert forces actively on the opposing antigen-presenting cell during activation. However, the molecular basis of force generation by T cells is poorly understood. Here, we report a molecular mechanism that involves the T-cell microtubule (MT) and actomyosin cytoskeletons, which interact through Rho GTPase activity. Our study highlights the role played by the MT cytoskeleton in regulating actomyosin-generated forces, which play a key role in T-cell activation.

Extraction by 1% Triton X-100 removed cytosolic proteins efficiently, preserving the centrosome, which was visible in TIRF illumination as a focal point from which MTs emanated (Fig. 1*A*). We found that MTs were largely contained within the F-actin meshwork at the periphery, consistent with a recent microscopy study of cytotoxic T-cell–APC conjugates (26). This cytoskeletal organization is reminiscent of the cytoskeletal organization in neuronal growth cones (28) and the leading edge of migrating cells (29), apart from the fact that the IS is relatively radially symmetric.

Although labeled tubulin provided an overall visualization of MT architecture, the cytosolic pool of free tubulin reduced the signal-to-noise ratio of the MTs, making the analysis of growing MTs in live cells challenging. We therefore transfected Jurkat T cells with end-binding protein 3 (EB3)-EGFP, which localizes to growing tips or plus-ends of MTs (30). As expected, in cells where the MTOC had presumably translocated to the contact zone, the centrosome appeared as a common initiation point for EB3 comets (Fig. 1*B* and Movie S2). Such extensive growth of MTs was specific to TCR stimulation, because cells plated on poly-L-lysine–coated coverslips showed very few EB3 comets in the beginning and almost no comets after 10 min of contact (Movie S3).

We tracked and quantified the position and instantaneous speed of growing MT tips (as marked by EB3-EGFP comets) using plusTipTracker software (30). To determine if these two parameters showed spatial dependence, we measured the radial and angular positions of these growing MT tips, defined by a polar coordinate system with the cell centroid as the origin (details are provided in *Materials and Methods*). The radial

distribution of tips differs significantly from the uniform ray model (Fig. S1*A*), in which MTs were assumed to emanate from the MTOC uniformly at all angles and to grow radially without hindrance. As shown in Fig. S1*B*, the empirical cumulative distribution function of the normalized radius significantly shifted to the left (Kolmogorov–Smirnov test: $P = 0$ between the experimental distribution and linearly distributed random radius), meaning that the cell center has high visit rates by growing MTs. Furthermore, by taking the ratio between the probability density functions (pdfs) of the experimental data and the uniform ray model ($\sim r$), we found that MT plus-tips are enriched near the cell center. The abundance of plus-tips decreases to a local dip when r reaches 0.6–0.7 and is abruptly abolished when $r > 0.9$ (Fig. S1*C*). Therefore, MT growth is regulated spatially, in which a minor "sink" is present near $r = 0.6$ and the cell periphery is a major sink.

In individual cells, we observed that the growth speed distribution remained nearly constant with activation time (Fig. S2*A*). We therefore pooled the individual tip speeds between the ninth and tenth minutes of contact in different cells to represent the overall MT growth speed. The speed distribution best fits a gamma distribution (χ^2 goodness of fit: $P = 9.4 \times 10^{-6}$; shape parameter: 1.38 ± 0.02; scale parameter: 76 ± 1 nm·s^{-1}; 17 cells, 25,554 comets; Fig. 1*C*), with the median speed $\pm$ quartile deviation given by 80 ± 53 nm·s^{-1}. For cells with the centrosome located reasonably close to the cell centroid (three examples are shown in Movie S2, with the approximate positions of the centrosomes labeled by the yellow circles), we found that the EB3 comets sped up when reaching out from the centrosome to a normalized radius of about 0.6–0.7 and slowed down significantly as they moved outward (Fig. S2*B*). To determine if MT growth speed is dependent on growth direction, we decomposed the instantaneous velocities into radial and tangential components. Both components showed no dependence on activation time (Fig. S2 *C* and *D*). Notably, the median angular velocities remained around zero, signifying no inherent helicities in the MT growth direction. On the other hand, we found that radial growth speed, but not angular speed, depends on the radial position (Fig. 1 *D* and *E*), confirming that the spatial regulation of MT growth is primarily in the radial direction. Because the F-actin network and dynamics vary significantly with the radial distance from the cell centroid (16, 31), this spatial dependence of MT speeds suggests that local actin architecture may modulate MT growth speed and direction.

Dynamic MTs Regulate Traction Stress Through Rho Kinase Activity. Our previous studies have shown that the actin cytoskeleton is important for force generation in T cells (9). To determine whether dynamic MTs also contribute to force generation, we used TFM to measure changes in traction stresses after small-molecule inhibition, as described in our earlier work (9). We used nocodazole (100 nM) or Taxol (500 nM) to inhibit MT growth. These doses have been previously used to study the mechanism of MTOC translocation during T-cell activation (7) and do not interfere with TCR signaling (32). Application of either of these two drugs to the cell after 10 min of activation rapidly decreased the number of dynamic MTs (Movie S4), although the decrease was more dramatic with nocodazole. We observed increased traction stresses after the addition of nocodazole, as indicated by the heat map (Fig. 2*A*). The stress ratio was calculated as the ratio of median stress in the time interval 9–15 min after drug treatment to the median stress in the time interval 0–3 min before drug treatment. Traction stress levels increased significantly upon inhibition of MT dynamics (40% for nocodazole, 20% for Taxol), as shown in Fig. 2*B* [stress ratio (median $\pm$ quartile deviation): 1.5 ± 0.5, $n = 31$ cells, Mann–Whitney U test: $P = 0.03$ for nocodazole; stress ratio $= 1.3 \pm 0.3$, $n = 30$ cells, $P = 0.05$ for Taxol; stress ratio $= 1.1 \pm 0.3$, $n = 75$ cells for
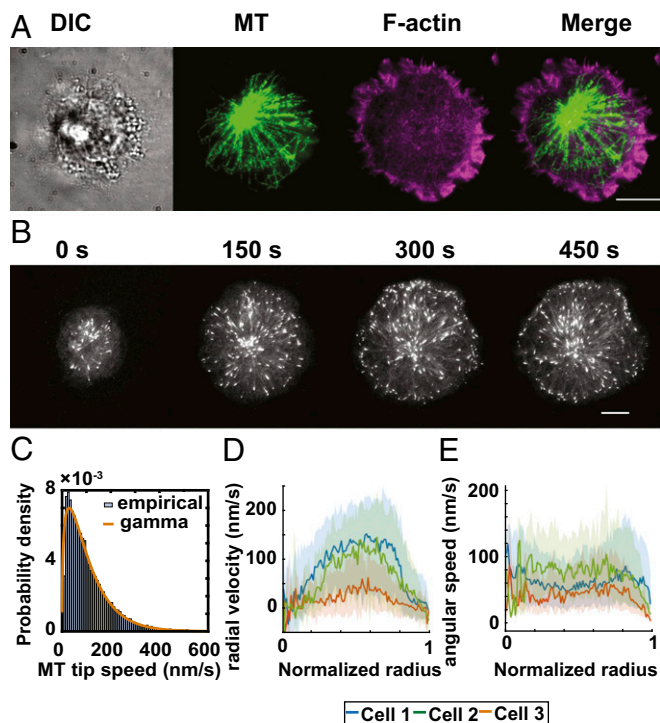

Fig. 1. MT dynamics in Jurkat cells upon activation. (*A*) E6-1 cell permeabilized and then fixed for 10 min and stained for tubulin (green) and F-actin (magenta). (*B*) Montage of E6-1 cells transfected with EB3-EGFP activated by anti-CD3. The centrosome is located approximately at the center of the frame. (*C*) Pdf of EB3 comet speed and its fit to gamma distribution. Radial (*D*) and tangential (*E*) velocities with the normalized radius for three representative cells shown in Movie S2 are illustrated. Solid lines represent the median, and shaded regions represent the range between the first and third quartiles. (Scale bars: 10 μm.)
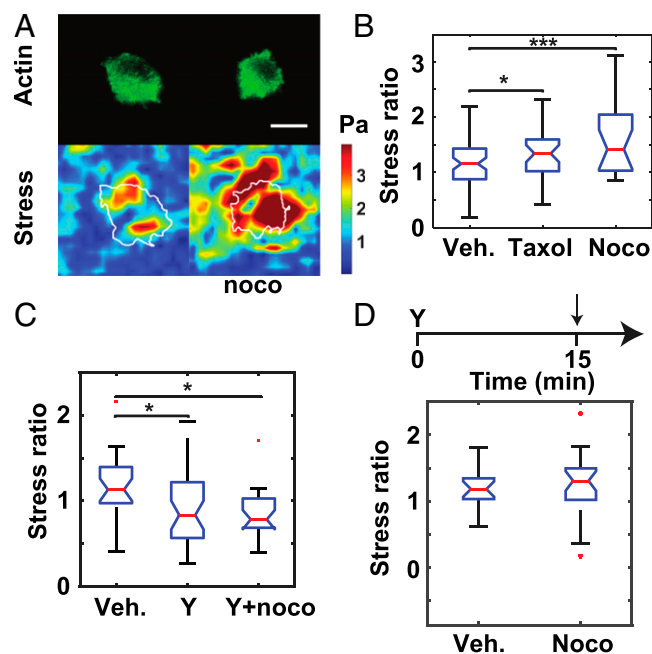
Fig. 2. Effects of MT inhibitors on traction stress. (*A*) EGFP-actin–labeled cells on anti-CD3–coated elastic substrates (*Top*) exert traction stresses (*Bottom*), which increase upon application of nocodazole (noco). (Scale bar: 10 μm.) (*B*) MT dynamics inhibition by 0.1 μM nocodazole and 0.5 μM Taxol both led to an increase in traction stress. (*C*) ROCK inhibition negated the stress-strengthening effect of nocodazole. (*D*) Stress ratios of vehicle (Veh.) vs. nocodazole treatments at 15 min after Jurkat cell spreading in the presence of 100 μM Y-27632. (*P < 0.05, ***P < 0.001; Mann–Whitney *U* test). Red dots indicate outliers (defined in *Materials and Methods*).

vehicle]. Although spreading is radially symmetrical, we note that the stress generation is heterogeneous over the contact zone potentially due to variations in cytoskeletal dynamics. Our previous work (9) has shown that there is significant signaling activation and cytoskeletal rearrangement while the traction stress reaches a plateau over this time interval.

Dynamic MTs have been shown to regulate Rho guanine nucleotide exchange factor (RhoGEF) activity, and the activation of Rho kinase (33, 34) and the Rho/Rho kinase (ROCK) pathway is known to regulate contractility in multiple cell types by modulating myosin phosphorylation (33, 35). We therefore hypothesized that the enhancement of traction stress by inhibition of MT dynamics might be caused by the up-regulation of Rho-ROCK activity, which would then increase contractility at the T-cell contact zone. If such were the case, simultaneous application of the ROCK inhibitor Y-27632 and nocodazole would negate the stress-strengthening effect of nocodazole alone. Consistent with our hypothesis, coapplication of 100 μM Y-27632 and 100 nM nocodazole resulted in a decrease in stress, to a similar extent as Y-27632 treatment alone (Fig. 2*C*; stress ratio = 0.8 ± 0.2, *n* = 23 cells, *P* = 0.03). To investigate whether MT dynamics are upstream of Rho signaling or whether they operate independently but have opposite effects on traction stresses, we examined if inhibition of MT dynamics increased traction stresses when ROCK activity was already suppressed. We activated Jurkat T cells on elastic substrates in the presence of Y-27632 for 15 min and then applied nocodazole. Nocodazole treatment did not increase traction stresses when ROCK was inhibited (Fig. 2*D*; nocodazole stress ratio = 1.2 ± 0.2, *n* = 25 cells, *P* = 0.8; vehicle stress ratio = 1.2 ± 0.2, *n* = 20 cells). This result indicates that these pathways do not regulate stress independently and that Rho-ROCK signaling lies downstream of dynamic MTs in regulating stress maintenance. Taken together,

our results suggest that dynamic MTs regulate traction stresses in T cells potentially through the Rho-ROCK pathway.

Dynamic MTs Regulate Nonmuscle Myosin II Phosphorylation. ROCK activation is known to lead to nonmuscle myosin II (NMII) light chain phosphorylation through the inhibition of myosin phosphatase (36, 37), which, in turn, leads to NMII assembly and clustering (35, 38). To elucidate the potential mechanism by which MT dynamics modulate force generation, we next investigated how ROCK activation and MT dynamics modulate NMII II accumulation and phosphorylation. We transfected Jurkat cells with EGFP-tagged myosin regulatory light chain (MLC-EGFP) and visualized NMII simultaneously with F-actin, MTs, and NMII heavy chain A (MYH9), using immunostaining as described earlier. NMII localized to the lamellar ring between the cell edge and the actin-sparse central region, forming an "NMII-rich zone" in the cell (Fig. S3*A*). Overlay with MTs revealed significant overlap between NMII and MTs in the lamella, indicating that the lamella was a potential zone where MT–actomyosin interactions could take place (Fig. S3*B*). Finally, we found that MYH9 localized to the periphery of the NMII ring (Fig. S3*C*).

Phosphorylation of MLC at threonine-18 and serine-19 promotes NMII bipolar filament assembly and ATPase activity in vitro (39, 40). Large-scale phosphoproteomics analysis has shown that serine-19 of MLC is the primary site of phosphorylation during T-cell activation (41). We therefore interrogated the localization of phosphorylated MLC (pMLC) with an antibody against mono-pMLC at serine 19. Upon permeabilization and fixation after 10 min of stimulation, we found that pMLC localized to the NMII-rich zone in the cell (Fig. 3*A*). Cells that exhibited higher levels of NMII filament assembly (as indicated by MLC intensity levels) showed significantly increased colocalization of pMLC with NMII filaments, as indicated by the positive correlation between MLC intensity in NMII-rich regions and the respective pMLC staining (Fig. 3*B*; *n* = 41 cells, regression slope > 0, *P* = 0.005; the indices are defined in *Materials and Methods*), confirming that MLC in these NMII-rich regions was phosphorylated.

To investigate the effect of ROCK activation and MT dynamics on pMLC levels at the contact zone, we treated cells with the respective inhibitors after 10 min of activation, and fixed them at 20 min. For Jurkat cells, Y-27632 treatment reduced pMLC levels, whereas nocodazole treatment resulted in increased pMLC levels (Fig. 3 *C* and *E* and Table S1). We obtained similar results for primary human CD4+ cells, in which Y-27632 treatment reduced pMLC levels and nocodazole treatment resulted in an increase in pMLC levels (Fig. 3 *D* and *F* and Table S2). We carried out two independent experiments for each cell type and observed similar results. This finding indicates that inhibition of MT dynamics (which increases traction stresses generated by T cells) positively correlates with pMLC levels at the activating cell-surface contact.

NMII Light Chain Phosphorylation Regulates Traction Stress. We next examined whether Rho signaling regulates traction stress maintenance through NMII phosphorylation. We used calyculin A (CA), a serine/threonine protein phosphatase inhibitor that inhibits myosin phosphatase activity (37, 42), at a concentration of 5 nM. CA treatment increased traction stresses after 15 min by 30% (Fig. 4 *A*, *B*, and *G*; stress ratio=1.4 ± 0.4, *n* = 23 cells, Mann–Whitney *U* test: *P* = 0.03). Because CA inhibits both type 1 and type 2A protein phosphatases, we used okadaic acid (OA), at a concentration that preferentially inhibits type 2A phosphatase (20 nM), as a negative control (42). The stress ratio after OA treatment did not differ from the stress ratio of vehicle significantly (*P* = 0.15), but it was lower than with CA treatment (stress ratio =0.9 ± 0.2, *n* = 15 cells, *P* = 0.007; Fig. 4 *C*, *D*, and *G*). Therefore, we infer that the effect of CA is most likely due to its inhibition of myosin phosphatase (a type 1 phosphatase) (43,
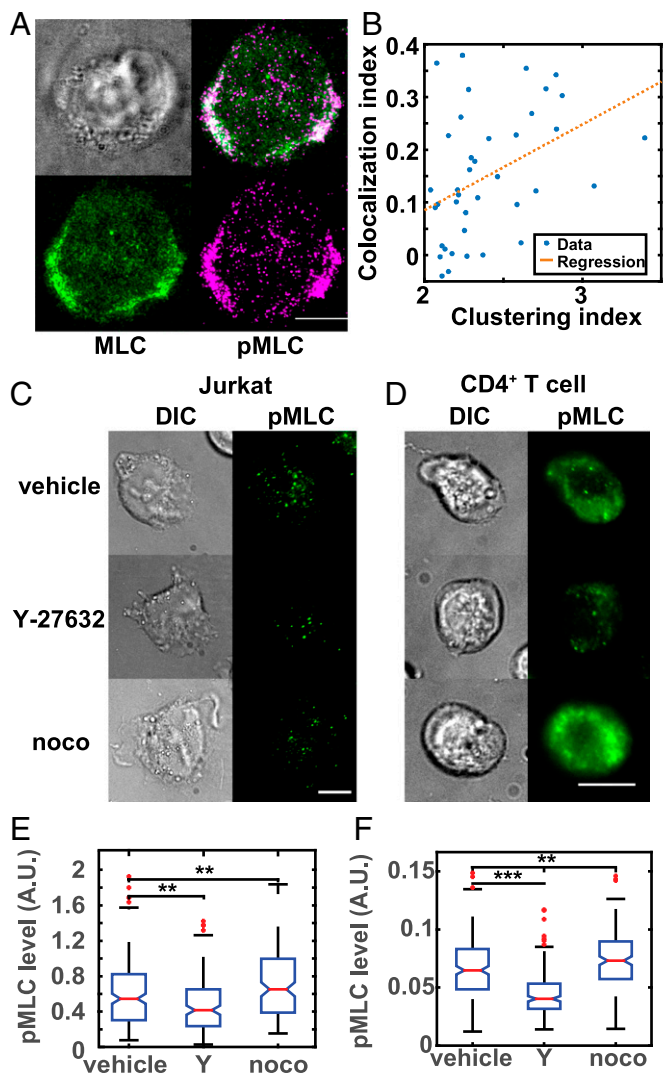
Fig. 3. MT dynamics regulate MLC phosphorylation. (*A*) Representative MLC-EGFP–expressing cell fixed at 10 min and stained for pMLC. (*B*) Cells with more NMII filament formation have higher pMLC colocalization with MLC. Bright-field differential interference contrast (DIC) microscopy and pMLC (green) images of Jurkat cells (*C*) and human CD4+ T cells (*D*) after treatments using the inhibitors indicated. Quantification of pMLC immunofluorescence intensity of Jurkat cells (*E*) and CD4+ human T cells (*F*) (**$P <$ 0.01, ***$P <$ 0.001; Mann–Whitney U test). Red dots indicate outliers (defined in *Materials and Methods*). (Scale bars: 10 μm.) A.U., arbitrary units.

44), and our data indicate that NMII contractility contributes to traction maintenance in Jurkat T cells.

Because myosin phosphatase activity lies downstream of Rho activity (36), we next examined whether the inhibition of myosin phosphatase could reverse the stress relaxation effects of ROCK inhibition by coapplication of CA and Y-27632 compared with the stress ratio upon application of Y-27632 alone. As shown in Fig. 4 *E–G*, CA reversed the effect of Y-27632 (stress ratio $= 1.0 \pm 0.4$, $n = 25$ cells, $P = 0.8$). Overall, our data suggest a positive correlation between ROCK-controlled NMII light chain phosphorylation and traction stress maintenance.

Regulation of Actomyosin Dynamics During Contact Formation. A number of studies have revealed a close connection between actomyosin dynamics and traction stresses exerted by the cell (45, 46). Given our observations of traction stress modulation, we proceeded to examine how the spatial distribution and

dynamics of the actomyosin cytoskeleton are regulated by MT dynamics and Rho kinase activity. TagRFP-T-actin–expressing Jurkat cells were transfected with MLC-EGFP to visualize both proteins simultaneously using TIRF. We observed that NMII accumulated and underwent retrograde flow that spanned the lamellar region (Fig. 5*A* and Movie S5). A closer look at the dynamics of these NMII-rich filaments indicated that they accumulated at the anterior, formed arcs while traveling in a retrograde manner, and disassembled upon reaching the posterior of the lamella (Movie S6). We quantified myosin intensity and retrograde flow speeds of actin and myosin as shown in the work flow in Fig. S4.

We found that the NMII TIRF intensity (blue) inside the contact zone, normalized by the respective average intensities measured in the 9- to 10-min time window, increased in the first 10 min and saturated thereafter, whereas actin intensity (red) stayed roughly constant (Fig. S5*A*). We defined the ratio of average intensity in the 9- to 10-min time window to average intensity in the 0- to 1-min time window as the "protein recruitment index." Comparison of protein recruitment indices showed that during cell spreading, the total actin content at the interface remained constant despite considerable polymerization/depolymerization dynamics (index $= 0.96 \pm 0.18$, $n = 111$ cells), whereas the NMII levels increased significantly with time (Fig. S5*B*; index $= 1.1 \pm 0.2$, $n = 180$ cells, Mann–Whitney U test: $P = 0.002$).

To quantify the retrograde flows of actin and NMII, we performed optical flow analysis of NMII and actin image sequences between consecutive frames (2.5- or 5-s interval) (Fig. S4 *D* and *G* and Movie S7). We calibrated the optical flow tracking results with the optical flow tracking results from simulated flow and kymography of live-cell image sequences (Fig. S4*J*). The pdfs of NMII and actin retrograde flow speed between 9 and 10 min of activation both showed a single peak (Fig. 5*B*). We found the NMII speed to be 17 ± 8 nm·s^{-1} (median $\pm$ quartile deviation; $n = 195,443$ vectors) and the actin speed to be 27 ± 14 nm·s^{-1}
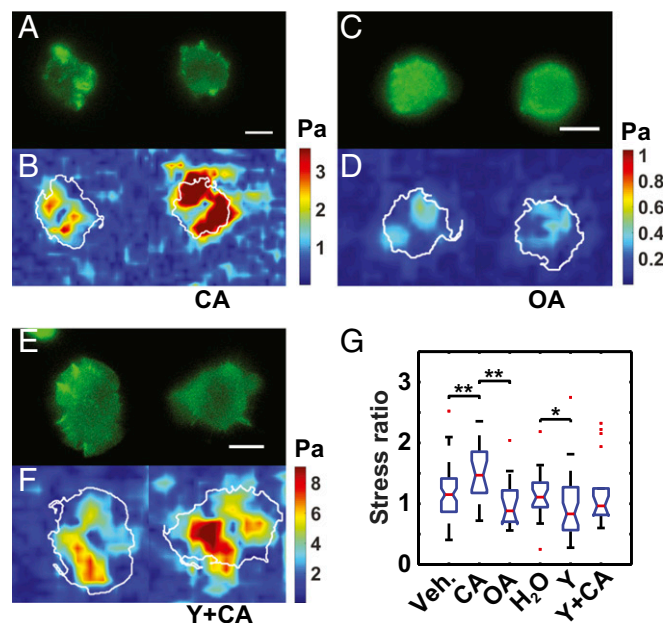

Fig. 4. Dissecting the role of myosin II in stress maintenance. EGFP-actin (*A*, *C*, and *E*) and stress (*B*, *D*, and *F*) exerted by the cell before (*Left*) and after (*Right*) application of 5 nM CA (*A* and *B*), 20 nM OA (*C* and *D*), and 100 μM Y-27632 and 5 nM CA (*E* and *F*, Y + CA) at 15 min are shown. (*G*) Stress ratio of Jurkat cells after application of different NMII inhibitors at 15 min (*$P <$ 0.05, **$P <$ 0.01; Mann–Whitney U test). DMSO and OA are the negative controls of CA, and H$_2$O is the negative control of Y and Y + CA. (Scale bars: 10 μm.)
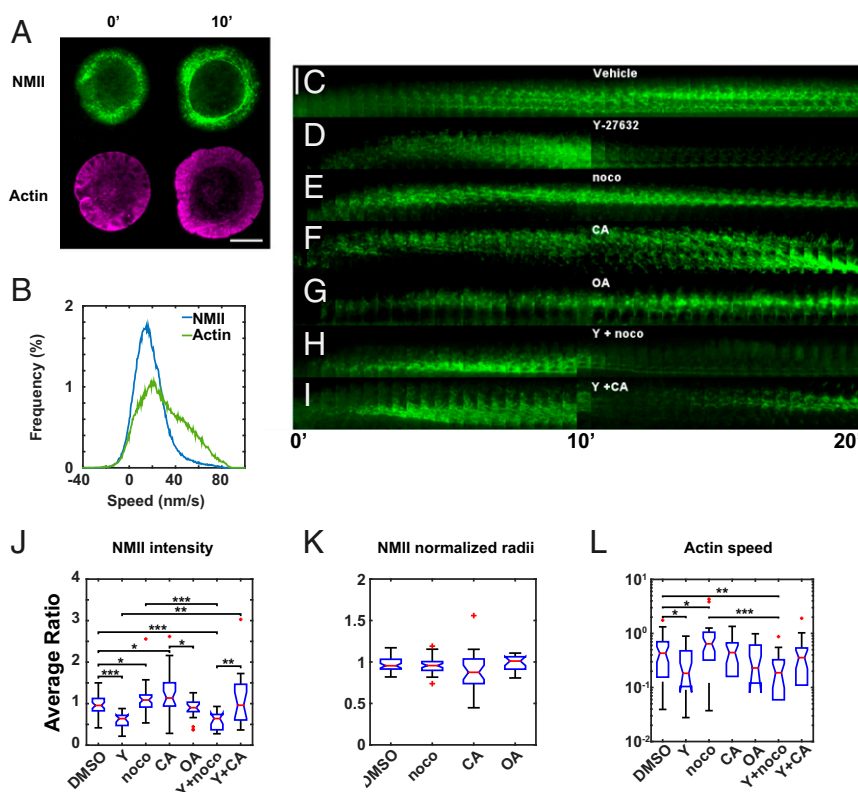
Hui and Upadhyaya

Fig. 5. NMII-rich actin-arcs dynamics are regulated by Rho signaling. (*A*) Montage of MLC-EGFP (green)– and TagRFP-T-actin (magenta)–transfected Jurkat cell spreading on an anti-CD3–coated coverslip imaged in TIRF mode. (Scale bar: 10 μm.) (*B*) PDF of actin (green) and NMII (blue) flow speeds at between 9 and 10 min of Jurkat T-cell activation. (*C–I*) Montages of a 30-s interval showing the dynamics of MLC-EGFP before and after application of the indicated inhibitors at 10 min. (Scale bar: 5 μm.) Average ratio of NMII intensity (*J*), NMII normalized radii (*K*), and actin flow speed (*L*) in the 19- to 20-min time interval after different drug treatments. (*P < 0.05, **P < 0.01, ***P < 0.001; Mann–Whitney *U* test). Red dots indicate outliers (defined in *Materials and Methods*).

(median ± quartile deviation; $n = 185,658$ vectors). To examine whether NMII speeds are correlated with actin speeds, we plotted NMII speeds (v_{NMII}) in various polar angles against the corresponding actin speeds (v_{actin}) (Fig. S5C). We found that the NMII/actin speed relation fit well with the formula: $v_{NMII} = v_0 e^{\sinh(\beta v_{actin} + \gamma)}$, with the hyperbolic sine function centered at $-\frac{\gamma}{\beta} = 48$ nm·s^{-1} and with a characteristic speed of $\frac{1}{\beta} = 19$ nm·s^{-1} (Fig. S5C; $n = 106$ cells, 1,400,981 NMII/actin speed pairs). The slope of the $v_{NMII} - v_{actin}$ curve about the center ($v_0 \alpha \beta$) was 0.34 and increased at higher v_{actin}, which agrees with kymography-based results in previous work that lamellar actin flow speeds are about 40% of the lamellipodial actin speeds (31).

We next examined the spatiotemporal regulation of actomyosin dynamics by MT dynamics, ROCK, and myosin phosphatase activity using pharmacological inhibition (Movie S8). To quantify the different aspects of actomyosin dynamics in the cell, we devised an additional parameter, the mean NMII normalized radius, in addition to NMII intensity and retrograde flow speeds of NMII and actin, respectively. As before, we applied inhibitors after 10 min of surface-bound anti-CD3 stimulation (montages of 30-s intervals of MLC-EGFP are shown in Fig. 5 *C–I*) and calculated the normalized value of each parameter (defined above) as the ratio of the parameter throughout the 10-min time window after drug application to the median of each parameter between 9 and 10 min of stimulation (right before drug application).

Using these ratios (Fig. 5 *J–M* and Fig. S6 *A–D*), we found that NMII intensity decreased upon inhibition of ROCK activity (Fig. 5J, Fig. S6A, and Table S3). Cotreatment with CA, but not nocodazole, restored NMII levels after 10 min (Fig. 5J, Fig. S6A, and Table S3). This result shows that Rho/ROCK activity is essential for the formation and maintenance of NMII filaments. CA treatment

alone increased NMII intensity (Fig. 5J, Fig. S6A, and Table S3), whereas OA treatment had no effect on NMII accumulation (Fig. 5J, Fig. S6A, and Table S3). Furthermore, nocodazole treatment led to an increase in NMII intensity (Fig. 5J, Fig. S6A, and Table S3), whereas coapplication of nocodazole with Y-27632 abrogated the increase (Fig. 5J, Fig. S6A, and Table S3). Overall, we found that the actomyosin ring dimensions were largely insensitive to inhibitors. However, CA treatment led to a slight, but statistically insignificant, inward contraction of the actomyosin ring (Fig. 5K, Fig. S6B, and Table S3). Therefore, myosin phosphatase may lead to the disassembly of NMII filaments, as expected for its MLC dephosphorylation activity.

We next quantified the effect of MT, ROCK, and phosphatase inhibition on peripheral actin flow. We found that application of nocodazole alone led to more sustained actin flow (Fig. 5L, Fig. S6D, and Table S3), whereas Y-27632 treatment and its coapplication with nocodazole negated this effect by suppressing peripheral actin flow (Fig. 5M), Notably, whereas CA treatment led to increased NMII intensity, the maintenance of actin flow was not affected (Table S3). However, coapplication of CA rescued the decrease due to Y-27632 application alone (Fig. 5M, Fig. S6D, and Table S3). These observations suggest that although peripheral actin flow is correlated with NMII contractility, inhibition of dynamic MTs could prolong actin flow in an NMII contractility-independent manner that cannot be recapitulated by inhibiting myosin phosphatase.

Actin Retrograde Flow Is Negatively Correlated with MT Arrival. Our observations suggest that local actin flow speed could be regulated by the presence of MTs in the region. We therefore transfected EB3-EGFP–expressing Jurkat cells into TagRFP-T-actin–expressing

Jurkat cells to image actin flow and MT growth simultaneously ([Movie S9](#)). Specifically, we were interested in the relationship between the MT influx into the peripheral region (normalized radius r: $0:8 < r < 1$) and local actin flow speed in that region. We counted the number of MT tracks that arrived at different polar angles at the periphery for all time points (Fig. 6 *A* and *B*). A rough estimate of MT influx is given by the accumulated number of MT arrivals divided by the time since first entry of MTs per unit area. When we pooled the analyzed MT influx (between 9 and 10 min of activation) and plotted it as a function of the local actin speed, we found that actin retrograde flow speed was negatively correlated with MT influx (number of cells analyzed = 17, number of flow vectors analyzed = 40,322; Fig. 6*C*). Therefore, MT growth into the periphery could be a "hidden" factor that modulates actin flow and potentially contributes to the intercellular and intracellular heterogeneities of actin flow speed (Fig. 5*B*).

To investigate further whether Rho signaling mediates the correlation between MT dynamics and actin flow, we focused on two key effectors of Rho: ROCK and formin. Notably, the formin, mDia1, is known to be activated upon Rho activation by a direct structural interaction (47). Furthermore, recent in vitro studies have shown that formins bind to MTs through their FH2 domain, which suppresses the actin polymerization function of formins (48, 49), although the formin mDia1 was also reported to polymerize actin filament by recruitment to MT tips (50). In addition, a recent study showed that NMII-rich actin arcs in the IS are derived from formin-mediated actin polymerization primarily in the lamellipodia (51). To test whether the activation of ROCK and formin mediates MT–actin interactions at the T-cell contact zone, we activated EB3-EGFP– and TagRFP-T-actin–expressing Jurkat cells on anti-CD3–coated coverslips in the presence of Y-27632 or the formin inhibitor SMIFH2 (15 µM) (52). SMIFH2 inhibits the actin polymerization activity of formins. Jurkat cells were able to spread in the presence of either inhibitor ([Movie S10](#)), and we observed an increase in MT growth speed in both cases (Fig. 6*D* and [Table S4](#)). ROCK and formin inhibition both led to small but significant decreases in actin flow speeds between 9 and 10 min after activation (Fig. 6*E* and [Table S4](#)). Comparing the relationship between actin speed and MT influx, both treatments resulted in a slowing down of actin flow compared with vehicle throughout the range of MT influx, but the negative correlation between actin flow and MT influx still persisted (Fig. 6*F*). These observations are consistent with the hypothesis that Rho activity is essential for maintaining peripheral actin flow and for mediating MT-actin cross-talk through ROCK and formin activation.

Discussion

Physical forces are known to regulate multiple cell biological processes (53). In the context of immune synapse formation, traction stresses generated by T cells enable antigen discrimination and cell activation (11), likely through the enhancement of interaction lifetime upon application of forces to the TCR (54). Previous work, including ours, has characterized these forces and shown that they are dependent on pMHC affinity (11), actin dynamics (9), TCR signaling and calcium influx (8, 55), cdc42 activity (11), and stiffness of the opposing substrate (9, 10, 56). Here, we integrate force measurements with dual-color TIRF imaging to propose a model of force generation in T cells: Dynamic MTs locally modulate NMII filament assembly; lamellipodial actin flow; and, thereby, force generation through the Rho GTPase pathway (Fig. 7). Our work has thus identified the interactions between MT and actomyosin cytoskeletal dynamics as critical determinants of force generation during T-cell activation.

Most previous studies on the role of MTs in T-cell activation have focused on the rapid translocation of the MTOC upon pMHC ligation (25, 26, 57) and the molecular mechanisms that underlie this process (5, 19, 21, 58), The consensus view from these studies has been that the MT cytoskeleton acts as a scaffold, holding lytic granules and guiding centrosomal reorientation toward the APC for directional secretion. Although stable MTs have been demonstrated to be essential for MTOC translocation, our work identifies a role for dynamic MTs in regulating force generation at the cell periphery. Based on our studies, as well as previous studies on the link between MT plus-tip dynamics and focal adhesions (59–62), we suggest the following conceptual model. Growing MT tips sequester RhoGEF, such as GEF-H1 (63). RhoA activation requires the release of RhoGEFs from dynamic MTs, which may occur during a catastrophe event. According to this model, a loss of dynamic MTs would result in reduced sequestration of RhoGEF, leading to an effective increase in RhoGEFs at the lamellipodial/lamellar region, as well as increased RhoA activation, myosin contractility, and enhanced traction stresses, as we observe upon application of nocodazole and Taxol (Fig. 2). The effect of Taxol on traction enhancement is more modest compared with nocodazole because Taxol has a milder effect on reducing dynamic MTs than nocodazole (as observed qualitatively from time-lapse images). Our results, however, do not entirely preclude the involvement of stable
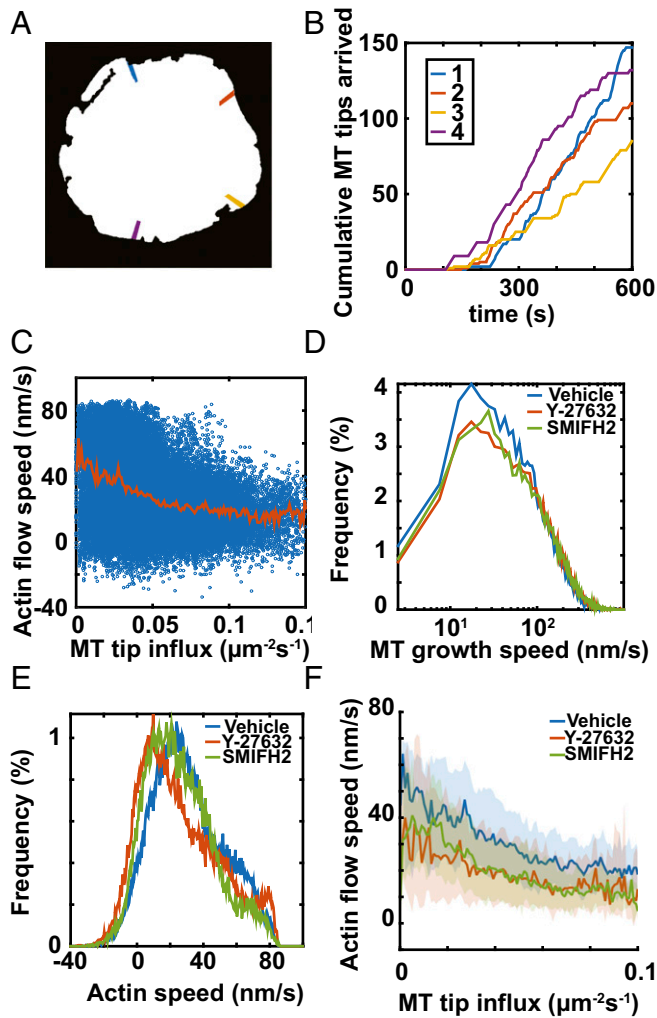

Fig. 6. MT influx suppresses local actin retrograde flow. (*A* and *B*) Cell contact and four regions of different polar angles in which the numbers of MTs entering each region were counted as a function of time. (*C*) Actin flow speed against MT influx in different polar angles. The pdfs of MT growth speed (*D*), actin flow speed (*E*), and the actin flow–MT influx relation for T cells spreading in the presence of vehicle and inhibitors (*F*) are shown. Data were taken at between 9 and 10 min of activation.
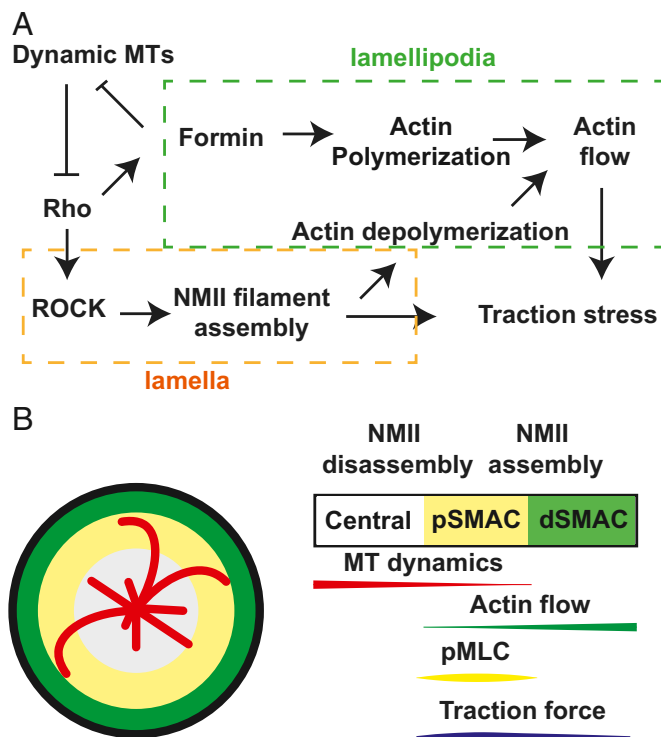
Fig. 7. Working model of MT dynamics-regulated contractility. (*A*) Working model of how MT dynamics regulate traction stress through the Rho-NMII-actin pathway. (*B*) Zones in T-cell contact according to cytoskeletal architecture, dynamics, and traction stress generation. dSMAC, distal supramolecular activation cluster; pSMAC, peripheral supramolecular activation cluster.

MTs, for example, with acetylated (19) and detyrosinated (21) tubulin, in regulating cellular contractility.

Our findings further define the role of NMII-mediated contractility in T-cell activation. NMII is essential for T-cell migration (64), especially in confined spaces (65). By combining TFM, live-cell imaging, and immunofluorescence, we have shown that Rho-ROCK activity is essential to maintain both pMLC levels and traction forces, linking force generation to MLC phosphorylation and filament assembly. Previous studies (16, 17) have examined actin flows during T-cell activation and the role of Rho-kinase activity and myosin IIA on modulation of these flows (16, 17). These studies showed that both inhibition of myosin IIA and actin disassembly are required to arrest actin retrograde flows that govern several aspects of signaling, such as microcluster dynamics, Ca^{2+} signaling, and PLC-γ1 phosphorylation. Our work adds to those results by elucidating the role of both the actomyosin machinery and dynamic MT activity on T-cell force generation and suggests the possible role of these forces in regulating T-cell signaling.

Our results further suggest that formin activation may be an additional pathway mediating MT-actin cross-talk. It has previously been shown that mDia1 deletion results in impaired T-cell development, proliferation, and migration (66). Our results suggest that formins regulate peripheral actin flow, presumably activated by local Rho activation to initiate actin polymerization (47), which, in turn, is regulated by local MT dynamics (Fig. 7). We favor actin polymerization over MT stabilization to be the dominant activity of formins in the cell periphery based on two observations: First, formin-mediated linear actin bundles have been demonstrated in the T-cell contact zone, with formins located near the cell edge (51), and, second, visits by MTs into the lamellipodia are rare (Fig. S1C). On the other hand, we cannot exclude the possibility that some dynamic MTs that visit the periphery might be stabilized by formins there.

Finally, other factors may also contribute to the interaction between actin and MTs to coordinate force generation (e.g., perturbation of ezrin-disrupted immune synapse shape) potentially by affecting the link between cortical actin and the MT network (67).

Although Rho appears to sit at the crossroads between MT and actomyosin dynamics and an inactivating G17V mutation in the RHOA gene is associated with angioimmunoblastic T-cell lymphoma (68), the links between TCR triggering and Rho activation remain to be investigated. A comprehensive study of activated signaling elements in T cells has shown that whereas cdc42 and, to a lesser extent, Rac1 are active at the periphery of the contact zone, where they generate lamellipodial actin dynamics, RhoA becomes more centralized (69). This more central location of RhoA activation overlaps with the actomyosin ring that we observe (Fig. 5). Regardless of the molecular mechanism of Rho activation, we speculate that an inward spatial gradient of Rho activity develops in the IS driven by MT dynamics. It is likely that all three Rho GTPases contribute to the development and maintenance of traction forces in distinct spatiotemporal patterns (70).

Our observations of actin arc and myosin ring assembly and contractility are likely to be a general feature of T-cell activation. A recent study of CD8$^+$ T cells conjugated with target cells using light sheet microscopy showed strong actin retrograde flows that are very similar to the flows observed in vitro on the coverslip systems (26). Furthermore, earlier studies have shown that IS formation is accompanied by large-scale retrograde flows and polarized myosin II accumulation toward the IS, with similar kinetics to what we observe here (71). Given the limitations of currently available imaging technologies for obtaining high spatial resolution views of subcellular structures at the cell–cell contact, actin arcs have not yet been observed in T-cell–cognate APC conjugates.

Our study also sheds light on the importance of the mechanical properties of the ligand-bearing surface in T-cell activation. T cells encounter APCs of varying stiffness, which is an important physiological aspect. In addition, although unligated pMHCs diffuse freely in dendritic cells (DCs) (72), pMHC ligation leads to polarized DC actin polymerization toward the T cell (73), impeding the diffusion of pMHCs and facilitating the formation of TCR-pMHC microclusters (74). Mechanical forces generated by the T cell are therefore likely to be transduced through the TCR-pMHC bond to the APC. Therefore, the stiffness of the APCs (75) is a potential key parameter that the T cell senses, and it also matches well with the stiffness of the soft substrates we used in this study.

In conclusion, our work establishes the importance of internal cytoskeletal dynamics in force generation in T-cell activation. We have shown that T cells use two mechanisms to generate and maintain traction stresses: actin flow at the periphery and NMII filament assembly-mediated contraction (Fig. 7). Both mechanisms are likely to be physiologically relevant, because the effects of ROCK and MT inhibition on the pMLC are observed in both Jurkat and primary human CD4$^+$ cells. How T cells use and modulate this pathway to achieve mechanosensing (76), as in the case of mesenchymal stem cells, remains to be understood. Interestingly, the lymph node itself is also mechanically active, because Rho inactivation in fibroblastic reticular cells enables lymph node expansion during inflammation (77). Understanding the mechanobiology of T-cell activation is important for immunotherapy design against cancer because the tumor microenvironment is known to undergo significant extracellular matrix remodeling and stiffness changes during disease progression (78). The molecular mechanisms linking cytoskeletal forces with TCR-mediated signaling initiation will be the subject of future investigation.

Materials and Methods

Cells and Reagents. Primary peripheral CD4$^+$ T cells were a generous gift from Janis Burkhardt, Children's Hospital of Philadelphia. Jurkat E6-1 cells and purified human CD4$^+$ T cells were cultured in RPMI 1640 supplemented with 10% FBS and 1% penicillin/streptomycin. The MLC-EGFP was a gift from

Hui and Upadhyaya

Robert Fischer, Laboratory of Cell and Tissue Morphodynamics, National Heart, Lung, and Blood Institute, Bethesda. It was transfected into TagRFP-T-actin–expressing E6-1 cells by electroporation.

Anti-CD3 (Hit3a) was purchased from eBioscience. Antibodies against tubulin, NMIIA, and monophosphorylated NMII light chain were purchased from Abcam. CA and antibody against doubly phosphorylated NMII light chain were purchased from Cell Signaling Technology. Y-27632 was purchased from SelleckChem. OA was purchased from Santa Cruz Biotechnology. Taxol was purchased from Cayman Chemical. Forty percent acrylamide, 2% Bis-acrylamide, ammonium persulfate, and tetramethylethylenediamine were purchased from Bio-Rad. FluoSphereRed microspheres (0.2 μm) were purchased from Molecular Probes. Poly-L-lysine and nocodazole were purchased from Sigma–Aldrich. Sylgard 164 elastomers were purchased from Ellsworth Adhesives. Stainless-steel microspheres were purchased from Salem Balls. Hydrazine hydrate and colchicine were purchased from Acros. L-15 medium was purchased from Life Technologies. All oligos were purchased from Integrated DNA Technologies.

Preparation of Elastic Substrates and Microscopy. The procedures for polyacrylamide gel preparation and TFM are as described previously (9). For immunofluorescence imaging, images of four different channels, namely, interference reflection microscopy (IRM), bright-field differential interference contrast microscopy, and green and red TIRF fluorescence, were acquired. At the end of an experiment, one image of fluorescent dextran solution was taken for shading correction and one image with all light sources turned off was taken for dark noise removal.

Immunofluorescence. Conventional fixation was carried out by fixing the cells with 2.4% paraformaldehyde (PFA) for 30 min at 37 °C; permeabilizing cells in 0.1% Triton X-100 for 4 min at room temperature; blocking cells with 2% normal goat serum for 30 min at room temperature; incubating cells with primary antibodies overnight at 4 °C; and, finally, incubating cells in secondary antibodies for 45 min at room temperature. The permeabilization before fixation protocol was adopted from previous studies (27). Cells were activated for a specified time period, and a 2× permeabilization buffer [10 mM 2-(N-morpholino)ethanesulfonic acid, 130 mM potassium chloride (KCl), 3 mM magnesium chloride (MgCl₂), 10 mM ethylene glycol tetraacetic acid, 2% Triton X-100, 8% polyethylene glycol 8000, 2% BSA] was added at a volume equal to the buffer the cells were in for 10 min at 37 °C. PFA was added to achieve a final concentration of 2.4% and fixed for 30 min.

Data Analysis. The TFM and cell edge tracking analysis procedure were previously described and were strictly followed in this work (2, 9). Unless specified otherwise, the Mann–Whitney U test was used for all statistical comparisons. Outliers were defined as data points more than three quartile deviations above the third quartile or below the first quartile.

EB3 Comet Tracking. We used u-track software (with the plusTiptracker module) for EB3 tracking (30). Radial and tangential speeds were calculated using the simple dot and cross-product between the instantaneous velocity vector and unit radial vector from the cell centroid.

Coordinate System to Characterize MT, NMII, and Actin Dynamics. The cell boundary was determined from the actin/IRM image sequence, and for each pixel inside the contact area, the normalized radius at that pixel was defined to be the ratio between the radial distance from the centroid to the distance between the centroid and the intersection point of the cell boundary with the extrapolated straight line from the centroid to the pixel (Fig. S4 *H* and *I*).

Recognition of NMII-Rich Regions. Background subtraction by morphological opening of the disk radius of 15 pixels (2 μm) was carried out on the NMII image sequence/immunofluorescence image. From each frame, the probability distribution of NMII background-subtracted intensity inside the cell was calculated, and the background (NMII-sparse regions) was modeled as either a Gaussian or a gamma, depending on which model gave a better fit and smaller mean squared error. The intensity range used for fitting was 2.5 σ above the background mean. After that point, the probability that the

observed NMII intensity was due to background noise was calculated for each pixel inside the cell contact, and a random number was drawn and compared with that probability. If the random number drawn was larger, the pixel was considered to be NMII-rich (Fig. S4C). In the analysis of MLC immunofluorescence, the background fluorescence of all cells was modeled as a Gaussian to ensure consistency.

Quantification of Colocalization Between MLC and pMLC. The pMLC dots were recognized by SpotDetector MATLAB software obtained from Francois Aguet, Broad Institute, Cambridge, MA. The Pearson correlation coefficient between MLC background-subtracted intensity and pMLC denoised intensity in pixels in which both signals are nonzero was defined to be the "colocalization index." The clustering index was defined to be the intensity ratio between MLC background-subtracted fluorescence inside and outside of the NMII-rich regions.

Quantitative Immunofluorescence. To analyze immunofluorescence images quantitatively, dark noise was first subtracted from each image. The image was then corrected for illumination shading by dividing with a dark noise-subtracted TIRF image of fluorescent dextran solution acquired at the end of imaging. Background fluorescence was then estimated from morphological opening of the disk radius of 120 pixels (26 μm) and was subtracted from the shading-corrected image to give the final quantitative image. Edges of single cells were tracked as previously described (2, 79). The average intensity in the tracked region was calculated for the channels of interest (green, red, or both).

Optical Flow Tracking for NMII and Actin. To ensure accuracy of the optical flow tracking software, we first produced a simulated image sequence of particle density 10 μm^{-2} at a defined speed between 0 and 200 nm·s^{-1} traveling in a positive x direction (Image Correlation Spectroscopy software from Cell Migration Gateway). The optical flow algorithm gives the flow speed vector $[u_{raw}(x; y; t); v_{raw}(x; y; t)]$ for every pixel (x, y) at all time points t. For every pixel $(x_0; y_0)$, we assume the speed vectors undergo smooth time evolution; therefore, we smoothed the flow vectors with respect to time: $u(x_0; y_0; t) = $ smooth $(u_{raw}(x_0; y_0; t))$, $v(x_0; y_0; t) = $ smooth $(v_{raw}(x_0; y_0; t))$. We found that moving the average of span 5 (25 s per 12.5-s window) gave the optimal result, compared with local regression-based methods, and that the algorithm gave accurate tracking of flow speed in the persistent flow simulation (Fig. S4J). In cells, actin/NMII flow often speeds up and slows down regularly, in which time-dimension smoothing could lead to underestimation of flow speed. We therefore obtained flow speed from kymographs of NMII/actin in live-cell image sequences and plotted those results against the flow speed from optical flow tracking (Fig. S4K). The relation was fitted with a hyperbolic tangent function $v_{kymo} = A \tanh (Bv_{OF})$. From this relationship, we can calibrate for underestimation of flow speed in the slow flow regime. All flow speed data shown in this report are calibrated.

Metrics to Quantify Actomyosin Dynamics. For every pixel in the NMII-rich region at each time point, the normalized radius, the polar angle of the pixel from the centroid, the background-subtracted intensity (NMII intensity), and the retrograde flow speed at that pixel were recorded. The median NMII intensity and mean normalized radius for all pixels inside the NMII-rich zone were obtained for every time point to represent the general behavior of the respective parameter in a cell. For actin flow, we used pixels inside the cell contact with a normalized radius between 0.8 and 1 to represent the periphery. Polar angle and retrograde flow speed were recorded for further analysis. Retrograde flow speed was defined to be the inward radial component (from the pixel to the centroid) of the flow vector at that pixel. For flow speed analysis of both NMII and actin, 3° angular bins were used for all cells to allow intercellular comparison. In addition, median flow speed in each angular bin was used to represent average flow speed in the bin.

1. Bunnell SC, Kapoor V, Trible RP, Zhang W, Samelson LE (2001) Dynamic actin polymerization drives T cell receptor-induced spreading: A role for the signal transduction adaptor LAT. *Immunity* 14:315–329.
2. Lam Hui K, Wang C, Grooman B, Wayt J, Upadhyaya A (2012) Membrane dynamics correlate with formation of signaling clusters during cell spreading. *Biophys J* 102:1524–1533.
3. Grakoui A, et al. (1999) The immunological synapse: A molecular machine controlling T cell activation. *Science* 285:221–227.
4. Monks CR, Freiberg BA, Kupfer H, Sciaky N, Kupfer A (1998) Three-dimensional segregation of supramolecular activation clusters in T cells. *Nature* 395:82–86.
5. Gomez TS, et al. (2007) Formins regulate the actin-related protein 2/3 complex-independent polarization of the centrosome to the immunological synapse. *Immunity* 26:177–190.
6. Stinchcombe JC, Majorovits E, Bossi G, Fuller S, Griffiths GM (2006) Centrosome polarization delivers secretory granules to the immunological synapse. *Nature* 443:462–465.
7. Yi J, et al. (2013) Centrosome repositioning in T cells is biphasic and driven by microtubule end-on capture-shrinkage. *J Cell Biol* 202:779–792.

8. Bashour KT, et al. (2014) CD28 and CD3 have complementary roles in T-cell traction forces. *Proc Natl Acad Sci USA* 111:2241–6.

9. Hui KL, Balagopalan L, Samelson LE, Upadhyaya A (2015) Cytoskeletal forces during signaling activation in Jurkat T-cells. *Mol Biol Cell* 26:685–695.

10. Husson J, Chemin K, Bohineust A, Hivroz C, Henry N (2011) Force generation upon T cell receptor engagement. *PLoS One* 6:e19680.

11. Liu Y, et al. (2016) DNA-based nanoparticle tension sensors reveal that T-cell receptors transmit defined pN forces to their antigens for enhanced fidelity. *Proc Natl Acad Sci USA* 113:5610–5615.

12. Liu B, Chen W, Evavold BD, Zhu C (2014) Accumulation of dynamic catch bonds between TCR and agonist peptide-MHC triggers T cell signaling. *Cell* 157:357–368.

13. Ma Z, Finkel TH (2010) T cell receptor triggering by force. *Trends Immunol* 31:1–6.

14. Ma Z, Janmey PA, Finkel TH (2008) The receptor deformation model of TCR triggering. *FASEB J* 22:1002–1008.

15. Pryshchep S, Zarnitsyna VI, Hong J, Evavold BD, Zhu C (2014) Accumulation of serial forces on TCR and CD8 frequently applied by agonist antigenic peptides embedded in MHC molecules triggers calcium in T cells. *J Immunol* 193:68–76.

16. Babich A, et al. (2012) F-actin polymerization and retrograde flow drive sustained PLCγ1 signaling during T cell activation. *J Cell Biol* 197:775–787.

17. Comrie WA, Babich A, Burkhardt JK (2015) F-actin flow drives affinity maturation and spatial organization of LFA-1 at the immunological synapse. *J Cell Biol* 208:475–491.

18. Wloga D, Gaertig J (2010) Post-translational modifications of microtubules. *J Cell Sci* 123:3447–3455.

19. Serrador JM, et al. (2004) HDAC6 deacetylase activity links the tubulin cytoskeleton with immune synapse organization. *Immunity* 20:417–428.

20. Thurston SF, Kulacz WA, Shaikh S, Lee JM, Copeland JW (2012) The ability to induce microtubule acetylation is a general feature of formin proteins. *PLoS One* 7:e48041.

21. Andrés-Delgado L, et al. (2012) INF2 promotes the formation of detyrosinated microtubules necessary for centrosome reorientation in T cells. *J Cell Biol* 198:1025–1037.

22. Efimov A, et al. (2008) Paxillin-dependent stimulation of microtubule catastrophes at focal adhesion sites. *J Cell Sci* 121:196–204.

23. Ezratty EJ, Partridge MA, Gundersen GG (2005) Microtubule-induced focal adhesion disassembly is mediated by dynamin and focal adhesion kinase. *Nat Cell Biol* 7:581–590.

24. Rape A, Guo WH, Wang YL (2011) Microtubule depolymerization induces traction force increase through two distinct pathways. *J Cell Sci* 124:4233–4240.

25. Martín-Cófreces NB, et al. (2012) End-binding protein 1 controls signal propagation from the T cell receptor. *EMBO J* 31:4140–4152.

26. Ritter AT, et al. (2015) Actin depletion initiates events leading to granule secretion at the immunological synapse. *Immunity* 42:864–876.

27. Medeiros NA, Burnette DT, Forscher P (2006) Myosin II functions in actin-bundle turnover in neuronal growth cones. *Nat Cell Biol* 8:215–226.

28. Schaefer AW, Kabir N, Forscher P (2002) Filopodia and actin arcs guide the assembly and transport of two populations of microtubules with unique dynamic parameters in neuronal growth cones. *J Cell Biol* 158:139–152.

29. Salmon WC, Adams MC, Waterman-Storer CM (2002) Dual-wavelength fluorescent speckle microscopy reveals coupling of microtubule and actin movements in migrating cells. *J Cell Biol* 158:31–37.

30. Applegate KT, et al. (2011) plusTipTracker: Quantitative image analysis software for the measurement of microtubule dynamics. *J Struct Biol* 176:168–184.

31. Yi J, Wu XS, Crites T, Hammer JA, 3rd (2012) Actin retrograde flow and actomyosin II arc contraction drive receptor cluster dynamics at the immunological synapse in Jurkat T cells. *Mol Biol Cell* 23:834–852.

32. Huby RD, Weiss A, Ley SC (1998) Nocodazole inhibits signal transduction by the T cell antigen receptor. *J Biol Chem* 273:12024–12031.

33. Chang YC, Nalbant P, Birkenfeld J, Chang ZF, Bokoch GM (2008) GEF-H1 couples nocodazole-induced microtubule disassembly to cell contractility via RhoA. *Mol Biol Cell* 19:2147–2153.

34. Meiri D, et al. (2012) Mechanistic insight into the microtubule and actin cytoskeleton coupling through dynein-dependent RhoGEF inhibition. *Mol Cell* 45:642–655.

35. Riento K, Ridley AJ (2003) Rocks: Multifunctional kinases in cell behaviour. *Nat Rev Mol Cell Biol* 4:446–456.

36. Kimura K, et al. (1996) Regulation of myosin phosphatase by Rho and Rho-associated kinase (Rho-kinase). *Science* 273:245–248.

37. Watanabe T, Hosoya H, Yonemura S (2007) Regulation of myosin II dynamics by phosphorylation and dephosphorylation of its light chain in epithelial cells. *Mol Biol Cell* 18:605–616.

38. Vicente-Manzanares M, Ma X, Adelstein RS, Horwitz AR (2009) Non-muscle myosin II takes centre stage in cell adhesion and migration. *Nat Rev Mol Cell Biol* 10:778–790.

39. Craig R, Smith R, Kendrick-Jones J (1983) Light-chain phosphorylation controls the conformation of vertebrate non-muscle and smooth muscle myosin molecules. *Nature* 302:436–439.

40. Kamisoyama H, Araki Y, Ikebe M (1994) Mutagenesis of the phosphorylation site (serine 19) of smooth muscle myosin regulatory light chain and its effects on the properties of myosin. *Biochemistry* 33:840–847.

41. Mayya V, et al. (2009) Quantitative phosphoproteomic analysis of T cell receptor signaling reveals system-wide modulation of protein-protein interactions. *Sci Signal* 2:ra46.

42. Ishihara H, et al. (1989) Calyculin A and okadaic acid: Inhibitors of protein phosphatase activity. *Biochem Biophys Res Commun* 159:871–877.

43. Yam PT, et al. (2007) Actin-myosin network reorganization breaks symmetry at the cell rear to spontaneously initiate polarized cell motility. *J Cell Biol* 178:1207–1221.

44. Zhang XF, Schaefer AW, Burnette DT, Schoonderwoert VT, Forscher P (2003) Rho-dependent contractile responses in the neuronal growth cone are independent of classical peripheral retrograde actin flow. *Neuron* 40:931–944.

45. Aratyn-Schaus Y, Oakes PW, Gardel ML (2011) Dynamic and structural signatures of lamellar actomyosin force generation. *Mol Biol Cell* 22:1330–1339.

46. Gardel ML, et al. (2008) Traction stress in focal adhesions correlates biphasically with actin retrograde flow speed. *J Cell Biol* 183:999–1005.

47. Otomo T, Otomo C, Tomchick DR, Machius M, Rosen MK (2005) Structural basis of Rho GTPase-mediated activation of the formin mDia1. *Mol Cell* 18:273–281.

48. Gaillard J, et al. (2011) Differential interactions of the formins INF2, mDia1, and mDia2 with microtubules. *Mol Biol Cell* 22:4575–4587.

49. Roth-Johnson EA, Vizcarra CL, Bois JS, Quinlan ME (2014) Interaction between microtubules and the Drosophila formin Cappuccino and its effect on actin assembly. *J Biol Chem* 289:4395–4404.

50. Henty-Ridilla JL, Rankova A, Eskin JA, Kenny K, Goode BL (2016) Accelerated actin filament polymerization from microtubule plus ends. *Science* 352:1004–1009.

51. Murugesan S, et al. (2016) Formin-generated actomyosin arcs propel T cell receptor microcluster movement at the immune synapse. *J Cell Biol* 215:383–399.

52. Rizvi SA, et al. (2009) Identification and characterization of a small molecule inhibitor of formin-mediated actin assembly. *Chem Biol* 16:1158–1168.

53. Janmey PA, McCulloch CA (2007) Cell mechanics: Integrating cell responses to mechanical stimuli. *Annu Rev Biomed Eng* 9:1–34.

54. Iskratsch T, Wolfenson H, Sheetz MP (2014) Appreciating force and shape—the rise of mechanotransduction in cell biology. *Nat Rev Mol Cell Biol* 15:825–833.

55. Hu KH, Butte MJ (2016) T cell activation requires force generation. *J Cell Biol* 213:535–542.

56. Basu R, et al. (2016) Cytotoxic T cells use mechanical force to potentiate target cell killing. *Cell* 165:100–110.

57. Huse M (2012) Microtubule-organizing center polarity and the immunological synapse: protein kinase C and beyond. *Front Immunol* 3:235.

58. Liu X, Kapoor TM, Chen JK, Huse M (2013) Diacylglycerol promotes centrosome polarization in T cells via reciprocal localization of dynein and myosin II. *Proc Natl Acad Sci USA* 110:11976–11981.

59. Grigoriev I, Borisy G, Vorobjev I (2006) Regulation of microtubule dynamics in 3T3 fibroblasts by Rho family GTPases. *Cell Motil Cytoskeleton* 63:29–40.

60. Stehbens S, Wittmann T (2012) Targeting and transport: how microtubules control focal adhesion dynamics. *J Cell Biol* 198:481–489.

61. Wittmann T, Bokoch GM, Waterman-Storer CM (2003) Regulation of leading edge microtubule and actin dynamics downstream of Rac1. *J Cell Biol* 161:845–851.

62. Wittmann T, Waterman-Storer CM (2001) Cell motility: Can Rho GTPases and microtubules point the way? *J Cell Sci* 114:3795–3803.

63. Takesono A, Heasman SJ, Wojciak-Stothard B, Garg R, Ridley AJ (2010) Microtubules regulate migratory polarity through Rho/ROCK signaling in T cells. *PLoS One* 5:e8774.

64. Jacobelli J, Chmura SA, Buxton DB, Davis MM, Krummel MF (2004) A single class II myosin modulates T cell motility and stopping, but not synapse formation. *Nat Immunol* 5:531–538.

65. Jacobelli J, et al. (2010) Confinement-optimized three-dimensional T cell amoeboid motility is modulated via myosin IIA-regulated adhesions. *Nat Immunol* 11:953–961.

66. Eisenmann KM, et al. (2007) T cell responses in mammalian diaphanous-related formin mDia1 knock-out mice. *J Biol Chem* 282:25152–25158.

67. Lasserre R, et al. (2010) Ezrin tunes T-cell activation by controlling Dlg1 and microtubule positioning at the immunological synapse. *EMBO J* 29:2301–2314.

68. Yoo HY, et al. (2014) A recurrent inactivating mutation in RHOA GTPase in angioimmunoblastic T cell lymphoma. *Nat Genet* 46:371–375.

69. Singleton KL, et al. (2009) Spatiotemporal patterning during T cell activation is highly diverse. *Sci Signal* 2:ra15.

70. Makrogianneli K, et al. (2009) Integrating receptor signal inputs that influence small Rho GTPase activation dynamics at the immunological synapse. *Mol Cell Biol* 29:2997–3006.

71. Wülfing C, Davis MM (1998) A receptor/cytoskeletal movement triggered by costimulation during T cell activation. *Science* 282:2266–2269.

72. Comrie WA, Li S, Boyle S, Burkhardt JK (2015) The dendritic cell cytoskeleton promotes T cell adhesion and activation by constraining ICAM-1 mobility. *J Cell Biol* 208:457–473.

73. Al-Alwan MM, et al. (2003) Cutting edge: Dendritic cell actin cytoskeletal polarization during immunological synapse formation is highly antigen-dependent. *J Immunol* 171:4479–4483.

74. Yokosuka T, et al. (2005) Newly generated T cell receptor microclusters initiate and sustain T cell activation by recruitment of Zap70 and SLP-76. *Nat Immunol* 6:1253–1262.

75. Bufi N, et al. (2015) Human primary immune cells exhibit distinct mechanical properties that are modified by inflammation. *Biophys J* 108:2181–2190.

76. Judokusumo E, Tabdanov E, Kumari S, Dustin ML, Kam LC (2012) Mechanosensing in T lymphocyte activation. *Biophys J* 102:L5–L7.

77. Acton SE, et al. (2014) Dendritic cells control fibroblastic reticular network tension and lymph node expansion. *Nature* 514:498–502.

78. Acerbi I, et al. (2015) Human breast cancer invasion and aggression correlates with ECM stiffening and immune cell infiltration. *Integrative Biol* 7:1120–1134.

79. Lam Hui K, Kwak SI, Upadhyaya A (2014) Adhesion-dependent modulation of actin dynamics in Jurkat T cells. *Cytoskeleton* 71:119–135.